AGU PUBLICATIONS

Geophysical Research Letters

RESEARCH LETTER
10.1002/2017GL073331

Key Points:
- Equatorial westward jets in the Indian Ocean develop in response to downwelling equatorial Rossby waves
- Downwelling equatorial Rossby waves maintain warm SST anomalies after intraseasonal convection begins
- Intraseasonal SST anomalies substantially cool when ocean currents associated with equatorial Rossby waves are removed

Correspondence to:
A. V. Rydbeck,
adam.rydbeck.ctr@nrlssc.navy.mil

Citation:
Rydbeck, A. V., T. G., Jensen, and E. S., Nyadjro (2017), Intraseasonal sea surface warming in the western Indian Ocean by oceanic equatorial Rossby waves, *Geophys. Res. Lett.*, *44*, doi:10.1002/2017GL073331.

Received 3 MAR 2017
Accepted 19 APR 2017
Accepted article online 28 APR 2017

Intraseasonal sea surface warming in the western Indian Ocean by oceanic equatorial Rossby waves

Adam V. Rydbeck[1], Tommy G. Jensen[2], and Ebenezer S. Nyadjro[3]

[1]American Society for Engineering Education, Washington, District of Columbia, USA, [2]Naval Research Laboratory, Ocean Dynamics and Prediction Branch, Stennis Space Center, Hancock County, Mississippi, USA, [3]Department of Physics, University of New Orleans, New Orleans, Louisiana, USA

Abstract A novel process is identified whereby equatorial Rossby (ER) waves maintain warm sea surface temperature (SST) anomalies against cooling by processes related to atmospheric convection in the western Indian Ocean. As downwelling ER waves enter the western Indian Ocean, SST anomalies of +0.15°C develop near 60°E. These SST anomalies are hypothesized to stimulate convective onset of the Madden-Julian Oscillation. The upper ocean warming that manifests in response to downwelling ER waves is examined in a mixed layer heat budget using observational and reanalysis products, respectively. In the heat budget, horizontal advection is the leading contributor to warming, in part due to an equatorial westward jet of 80 cm s^{-1} associated with downwelling ER waves. When anomalous currents associated with ER waves are removed in the budget, the warm intraseasonal temperature anomaly in the western Indian Ocean is eliminated in observations and reduced by 55% in reanalysis.

1. Introduction

The temperature of the oceanic mixed layer (ML) is regulated by horizontal advection, radiative/heat fluxes, vertical advection, entrainment, mixing, and diffusion. On intraseasonal time scales, the tropical ML temperature (MLT) varies by 0.6°C from peak to peak in the Indian and Pacific Oceans in association with the Madden-Julian Oscillation (MJO) [*Madden and Julian*, 1972; *Drushka et al.*, 2012; *Halkides et al.*, 2015]. Similarly, intraseasonal sea surface temperature (SST) variations of 0.6°C are associated with the MJO, neglecting diurnal temperature variations that can exceed 2.0°C [e.g., *Moum et al.*, 2014; *de Szoeke et al.*, 2015; *Ruppert and Johnson*, 2014]. Surface fluxes are primarily responsible for patterns of SST/MLT warming and cooling in these studies. SST is observed to maximize just ahead of MJO convection. After convection begins, SST rapidly cools and reaches a minimum ~5 days later.

However, several studies have observed a certain class of MJO events that deviate from the previously observed relationship of intraseasonal convection and SST anomalies. For these select MJO events, convective onset is observed to be synchronized with downwelling equatorial Rossby (ER) waves in the western Indian Ocean (IO) [*Webber et al.*, 2010, 2012b; *Rydbeck and Jensen*, 2017]. As downwelling ER waves enter the western IO, warm SST anomalies phase lock with enhanced convection, in defiance of anomalous cooling by surface fluxes. Downwelling ER waves and the associated warm SST anomalies are hypothesized to initiate and grow MJO convection by driving convergence in the atmospheric boundary layer and enhancing surface heat fluxes. The SST-driven convergence leads deep convection by several days and is hypothesized to trigger MJO convection [*Rydbeck and Jensen*, 2017].

The synchronization of intraseasonal warm SST and enhanced convection anomalies during MJO initiation appears to be unique to the western IO. *Demott et al.* [2016] observed that warm SST anomalies in the western IO are also collocated with anomalously increased amounts of moist static energy. *Rydbeck and Jensen* [2017] showed that horizontal convergence of moisture, associated with downwelling ER waves, is important for boundary layer moisture buildup that precedes MJO initiation. The phase relationship of warm SST anomalies and enhanced MJO convection evolves as the MJO propagates eastward in the IO, suggesting that the role of SST anomalies varies as a function of the MJO lifecycle [*Gutzler et al.*, 1994; *Sperber et al.*, 1997; *Webber et al.*, 2010, 2012b; *de Szoeke et al.*, 2015; *Demott et al.*, 2016; *Rydbeck and Jensen*, 2017].

In this study, we describe a process by which warm intraseasonal SST anomalies develop and are maintained in the western IO, against the effects of cooling by surface fluxes. By analyzing the ML heat budget, we demonstrate that downwelling ER waves induce strong horizontal currents, including an equatorial

westward jet. These currents drive horizontal advection that is critical to the growth and maintenance of warm SST anomalies prior to and during MJO convective onset. Because ER waves require ~75 days to cross the IO [*Webber et al.*, 2010, 2012a, 2012b; *Gottschalck et al.*, 2013; *Rydbeck and Jensen*, 2017], the predictability of MJO events associated with ER waves might be extended by a similar amount of time.

2. Data and Methods

A combination of observational and reanalysis data that covers a 20 year period from January 1993 to December 2012 is used to examine intraseasonal SST warming associated with ER waves. Observed sea surface height (SSH) anomalies are obtained from Archiving, Validation, and Interpretation of Satellite Oceanographic data (AVISO) (0.25°) [*Pascual et al.*, 2006]. SST from the National Oceanic and Atmospheric Administration (NOAA) daily optimum interpolation V2 that includes a combination of advanced very high resolution radiometer (AVHRR) and Advanced Microwave Scanning Radiometer–Earth Observing System (AMSR-E) are used in observational composites [*Reynolds et al.*, 2007]. The AMSR-E/AVHRR data are used for June 2002–October 2011, and the AVHRR-only data are used for the remainder of the 1993–2012 period. Currents from Ocean Surface Current Analysis Real-time (OSCAR) (1/3°) [*Bonjean and Lagerloef*, 2002, *Earth Space Research*, 2009] are linearly interpolated from pentad to daily data for use in compositing with other daily data. OSCAR currents represent average currents in the upper 30 m of the ocean. TropFlux surface heat and radiative fluxes [*Praveen Kumar et al.*, 2012] are used to compute the net fluxes in the observed ML heat budget. NOAA outgoing longwave radiation (OLR) data (2.5°) [*Liebmann and Smith*, 1996] are used as a proxy for atmospheric convection.

SSH, temperature, and currents from the Hybrid Coordinate Ocean Model (HYCOM) Navy Coupled Ocean Data Assimilation (NCODA) reanalysis (1/12°) [*Metzger et al.*, 2014] are also used for comparison with observations. Climate Forecast System Reanalysis (CFSR) [*Saha et al.*, 2010] surface fluxes are used when calculating the ML heat budget for HYCOM reanalysis. ML depth (MLD) is computed from HYCOM reanalysis using the fixed density criterion of 0.125 kg m^{-3} referenced from the surface. The MLD is used in the calculations of the ML heat budget in both HYCOM and observations. These results are not significantly different when other MLD criteria are used.

Downwelling ER waves in the western IO are identified using the method of *Rydbeck and Jensen* [2017]. To briefly summarize their method, SSH anomalies from AVISO are filtered in wave number-frequency space to remove signals outside of 50–500 day periods and planetary zonal wave numbers −1 to −30 such that ER wave signals are largely isolated. The filtered SSH anomalies are averaged from 6°S–6°N and 59°E–69°E. The resulting time series is used as an ER wave index for compositing periods of robust downwelling ER waves. Events greater than 1.5 standard deviations are used for compositing, with the maximum for each event set as lag 0 days. The dates of the ER wave events are shown in Table 1 of *Rydbeck and Jensen* [2017], of which the first 14 events are included in this study. Intraseasonal anomalies are calculated by removing the seasonal cycle and applying a 20–200 day Lanczos band-pass filter with 241 weights.

3. Equatorial Rossby Waves and Westward Jets

Composites of unfiltered SSH anomalies and currents at lags −60 and 0 days are shown (Figure 1) for AVISO SSH anomalies and OSCAR currents (left column) and HYCOM SSH anomalies and surface currents (right column). At lag −60 days (Figures 1a and 1b), an eastward jet extends across much of the IO in both OSCAR and HYCOM data. The eastward jet is confined along the equator and is associated with an eastward propagating Kelvin wave that is downwelling on its leading edge as indicated by the SSH maxima in the eastern IO. These are commonly referred to as Yoshida-Wyrtki jets and are forced by surface westerly winds [*Yoshida*, 1959; *Wyrtki*, 1973]. *Rydbeck and Jensen* [2017] observed that the downwelling Kelvin wave in Figures 1a and 1b is forced by a combination of the semiannual intermonsoon and MJO westerlies. In HYCOM, the magnitude of SSH anomalies associated with the Kelvin wave in the central and eastern IO is weaker than observations, and negative SSH anomalies associated with upwelling ER waves in the western IO are stronger than observations. This is partly attributed to differences in the climatology used to calculate the respective SSH anomaly fields.

After reaching Sumatra, the Kelvin wave is partly reflected as poleward propagating coastal Kelvin and westward propagating downwelling ER waves. The forcing and resonance of semiannual Kelvin and ER waves in the IO has been represented in numerous models of varying complexity [i.e., *Cane and Sarachik*, 1981;

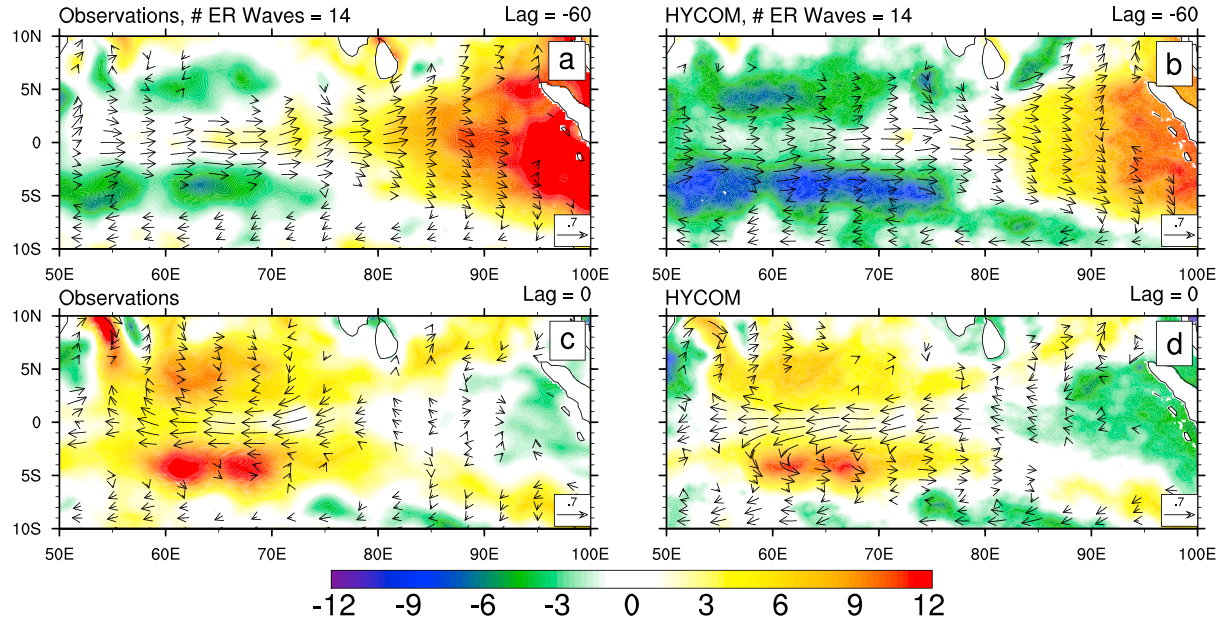

Figure 1. Composites of unfiltered SSH anomalies (shading; cm) and currents (vectors; m s^{-1}) are shown for (a and b) lag −60 and (c and d) lag 0 days. AVISO SSH and OSCAR currents are shown in Figures 1a and 1c. HYCOM SSH and surface currents are shown in Figures 1b and 1d. The reference vector is shown in the bottom right of each panel. Vectors with magnitudes less than 0.05 m s^{-1} are omitted.

Jensen, 1993; *Han et al.*, 1999]. The resultant downwelling ER waves are associated with local SSH maxima that flank the equator near 4°N/S and arrive in the western IO at lag 0 days (Figures 1c and 1d). Positive SSH anomalies are stronger in the southern hemisphere than the northern hemisphere in both data. However, HYCOM reanalysis slightly underestimates the SSH magnitude, and this may be related to the weaker downwelling Kelvin wave at lag −60 days. Along the equator and between the SSH maxima, an equatorial westward jet is present at lag 0 days. Westward jets associated with downwelling ER waves were first observed and described by *Delcroix et al.* [1991] in the Pacific Ocean. Westward jets have been observed to exceed 0.8 m s^{-1} in the Indian and Pacific Oceans [*Delcroix et al.*, 1991] but are weaker than the 1 m s^{-1} and greater speeds observed for Yoshida-Wyrtki jets in the IO [*Wyrtki*, 1973; *Knox*, 1976; *McPhaden*, 1982; *Han et al.*, 1999; *Moum et al.*, 2014; *Jensen et al.*, 2015]. While the Yoshida-Wyrtki jet spans most of the IO, the zonal extent of the westward jet is confined to the half wavelength of the ER wave.

The westward transit of ER waves across the IO is analyzed using composites of AVISO and HYCOM SSH anomalies averaged from 6°S to 6°N (Figures 2a and 2b). Positive SSH anomalies associated with downwelling ER waves originate near the coast of Sumatra and propagate westward at 0.9 m s^{-1}, consistent with the first meridional, first baroclinic mode ER wave. After weakening in the central IO, downwelling ER waves reemerge in the western IO with increasingly positive SSH anomalies. The arrival of downwelling ER waves in the western IO is coincident with the local development of negative intraseasonal OLR anomalies, as previously observed in other studies [*Webber et al.*, 2010, 2012b; *Rydbeck and Jensen*, 2017]. While the SSH maxima in HYCOM are ~40% weaker than observations in the eastern IO at lag −30 days, the maxima are comparable as the wave arrives in the western IO at lag 0 days.

In Figures 2c and 2d, a westward equatorial jet is observed to propagate along the path of downwelling ER waves. The westward jet maximizes in the central and western IO between lags −25 and 0 days and is stronger by ~30% in HYCOM, in part due to HYCOM's greater resolution [*Joseph et al.*, 2012]. Near the leading edge of the westward jet, between lags 5 and 10 days at 60°E, HYCOM MLT and NOAA SST anomalies are a local maximum. As discussed in the introduction, this local SST maximum is hypothesized to be partly responsible for MJO convective onset by driving boundary layer convergence and enhancing surface heat fluxes [*Webber et al.*, 2010, 2012b; *Rydbeck and Jensen*, 2017]. The observed SST maximum is 0.15°C, while the corresponding MLT anomaly in HYCOM is 0.12°C (Figures 2c and 2d). The HYCOM SST maximum (not shown) is similar in magnitude and location to the HYCOM MLT maximum, suggesting that SST may be used as a proxy for MLT. This relationship is utilized to compute the observed ML heat budget in the next section. In

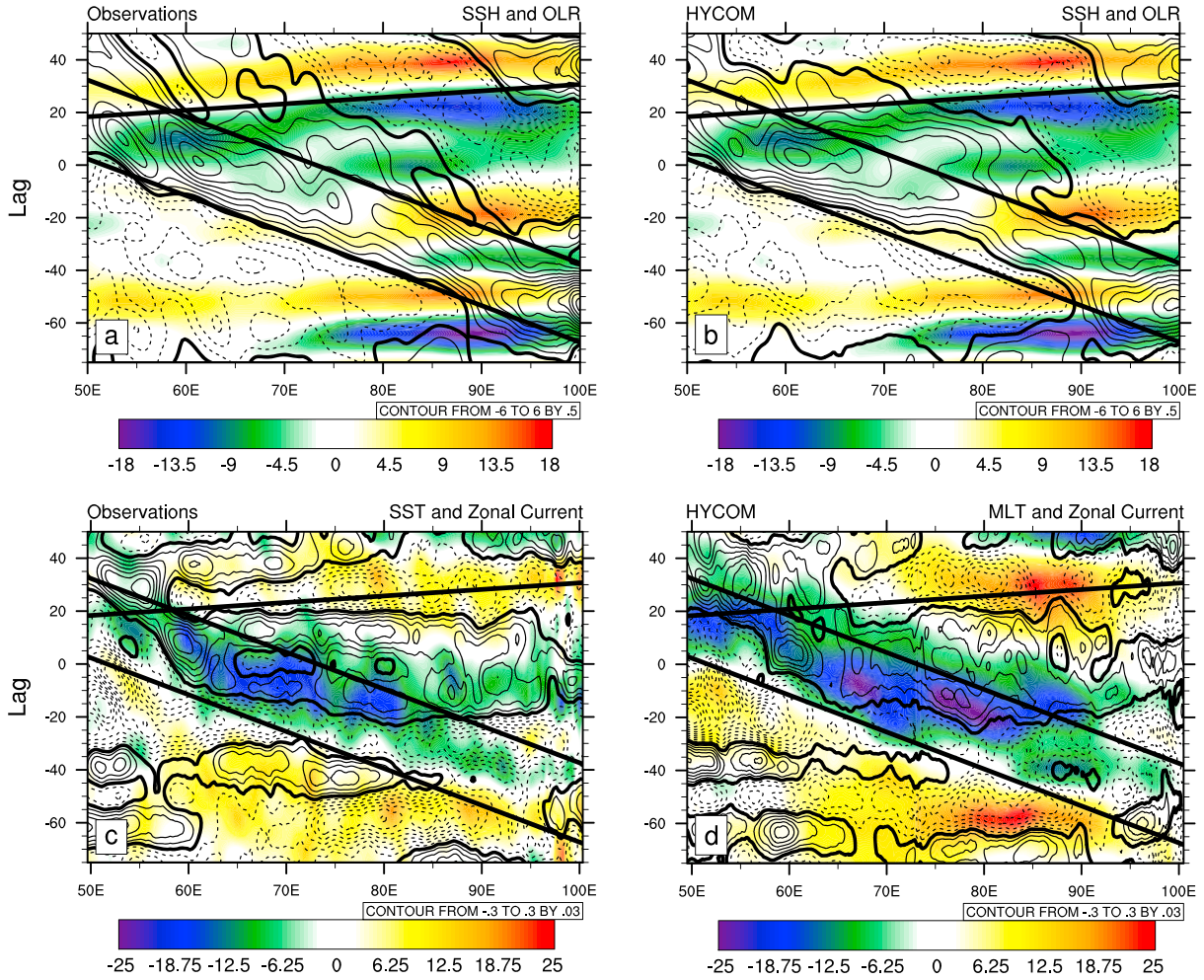

Figure 2. Composites of 20–200 day band-pass filtered (a) NOAA OLR (shading; W m^{-2}) and AVISO SSH (contours; cm) anomalies, (b) NOAA OLR and HYCOM SSH anomalies, (c) OCSCAR zonal current (shading; m s^{-1}) and NOAA SST (contours; °C) anomalies, and (d) HYCOM ML zonal currents (shading; m s^{-1}) and MLT (contours; °C) anomalies. SSH, SST, and OLR anomalies are averaged from 6°S to 6°N. Zonal current anomalies are averaged from 3°S to 3°N. Phase lines of 0.9 m s^{-1} westward and 5.0 m s^{-1} eastward are indicated by bold black lines. Positive (negative) contours are solid (dashed), and the contour interval is shown at the bottom right of each panel. The zero contour is bold.

observations, the SST maximum and OLR minimum near 60°E are largely in phase. Similar phasing of the SST maximum and OLR minimum is also observed in HYCOM. The continued warming of SST in the western IO after convective onset in both data is a remarkably interesting feature of the ER wave composites. To further examine the process by which intraseasonal SST anomalies warm in the presence of enhanced MJO convection, composite ML heat budgets for observations and reanalysis are analyzed, respectively.

4. Mixed Layer Heat Budget

The hypothesis by which robust downwelling ER waves trigger MJO convective onset hinges on the emergence of warm SST anomalies in the western IO. These anomalies are critical to the SST configuration that accounts for up to 45% of the intraseasonal atmospheric boundary layer convergence [*Rydbeck and Jensen*, 2017]. To determine whether SST anomalies in the region are generated as a result of horizontal advection, surface fluxes, processes related to the vertical velocity such as vertical mixing or Ekman pumping, or any combination thereof, an ML heat budget is calculated using observations and reanalysis, respectively, to better approximate the range of possible solutions. Because observations of the ML are scant over the region and period of interest, ML currents and MLT are estimated using OSCAR currents and NOAA SST. In HYCOM reanalysis, average ML current and temperature are utilized.

The intraseasonal ML heat budget is written as

$$\left(\frac{\partial \mathrm{MLT}}{\partial t}\right)' = -(U\cdot\nabla \mathrm{MLT})' + (Q_S)' + R \quad (1)$$

In this equation, primed terms are band-pass filtered for 20–200 days to capture the intraseasonal signals appropriate for ER wave and MJO time scales. The time tendency of the MLT, $\left(\frac{\partial \mathrm{MLT}}{\partial t}\right)'$, is determined by horizontal advection, $-(U\cdot\nabla \mathrm{MLT})'$, scaled net surface flux, $(Q_S)'$, and the residual, R. The net surface flux includes latent heat, sensible heat, longwave radiative, and net shortwave radiative fluxes and is scaled by the MLD and volumetric heat capacity of seawater. Net shortwave radiative flux is determined as the incoming shortwave radiative flux less the portion that penetrates the base of the ML, as calculated in *Pacanowski and Griffies* [1998]. Confidently calculating processes related to vertical motions is difficult using reanalysis and not achievable using observations for the region and time periods of interest. As a result, the residual, R, includes temperature tendencies due to Ekman pumping, entrainment, vertical mixing/diffusion, and any errors in the calculation of the other terms. The ML heat budget terms are averaged from 6°S–6°N, 58°E–62°E (see box in Figure 4) to capture the warming coincident with MJO convective initiation.

In the observations, the MLT increases by 0.28°C, from −0.16°C at lag −23 days to 0.12°C at lag +8 days (Figure 3a). Similar to the observations, the MLT in HYCOM increases by 0.25°C, from −0.14°C at lag −23 days to 0.11°C at lag +5 days. In both, the warm MLT anomaly is sustained for several weeks. The largest contributor to MLT warming in both budgets is horizontal advection, with a maximum value of 0.012 K d^{-1} at lag +1 day in observations and 0.011 K d^{-1} at lag −3 days in HYCOM. The respective contributions by zonal and meridional advections are comparable (not shown). Net surface fluxes from TropFlux and CFSR contribute to MLT warming prior to convection but act to cool MLT after convection begins near lag +2 days (see Figures 2a and 2b). Between lag −10 and +20 days, the residual in observations mostly contributes to MLT cooling. The residual in HYCOM also contributes to cooling between lag +3 and +15 days. However, the residuals in observations and HYCOM are out of phase prior to lag +2 days, suggesting different roles for unresolved processes at the leading edge of downwelling ER waves.

The prominent role of horizontal advection in both budgets suggests that circulations driven by ER waves are responsible for much of the intraseasonal warming in the western IO. To quantify the magnitude of the warming resulting from advection by intraseasonal currents, of which ER waves are the leading contributor, the horizontal advection term is separated into contributions from intraseasonal and nonintraseasonal currents:

$$-(U\cdot\nabla \mathrm{MLT})' = -\left(U'\cdot\nabla \mathrm{MLT}\right)' - \left(\left(U-U'\right)\cdot\nabla \mathrm{MLT}\right)' \quad (2)$$

Primed quantities indicate intraseasonal anomalies. The term on the left-hand side of equation (2), $-(U\cdot\nabla \mathrm{MLT})'$, is the horizontal advection. The first term on the right-hand side (RHS) of equation (2), $-(U'\cdot\nabla \mathrm{MLT})'$, is the horizontal advection resulting from the intraseasonal currents. The second term on the RHS of equation (2), $-((U-U')\cdot\nabla \mathrm{MLT})'$, is the horizontal advection by nonintraseasonal currents. Nonintraseasonal currents include high-frequency variability less than 20 days and low-frequency variability greater than 200 days.

Figures 3c and 3d show select terms of the ML heat budget with (dashed) and without (solid) horizontal advection by intraseasonal currents, $-(U'\cdot\nabla \mathrm{MLT})'$. In observations, horizontal advection and the MLT tendency are weakened by ~70% at lag 0 days when intraseasonal currents are removed (Figure 3c). The contributions to horizontal advection by the zonal and meridional intraseasonal currents are comparable (not shown), indicating that the meridional currents are as important as the westward jet. The dramatic reduction of the MLT tendency results in an MLT maximum that is weakened to near zero and shifted to earlier lags by 3 days. From these results, the role of intraseasonal currents associated with ER waves is to warm the MLT and shift it to later lags. This method does not remove all effects of ER waves on the MLT tendency and anomaly. For example, processes such as vertical advection and mixing by ER waves remain.

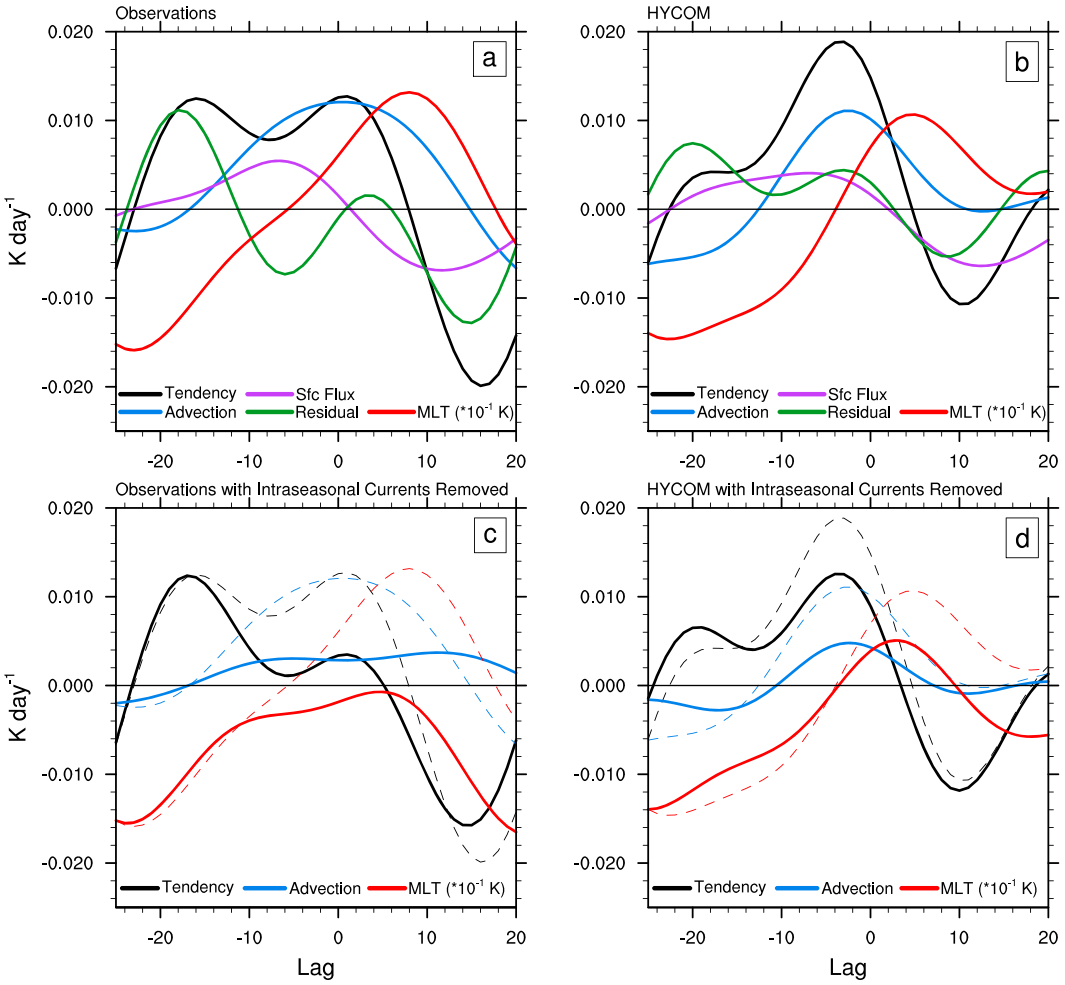

Figure 3. Intraseasonal ML heat budget terms averaged from 6°S–6°N, 58°–68°E are shown for (a and c) observations and (b and d) HYCOM reanalysis. In Figures 3a and 3b, all terms in equation (1) are shown. In Figures 3c and 3d, horizontal advection by intraseasonal currents is removed from the MLT tendency, horizontal advection, and MLT and is shown in solid lines. The dashed lines indicate the corresponding complete terms shown in Figures 3a and 3b. In each panel, MLT anomalies are multiplied by 10^{-1}.

When intraseasonal currents are removed in HYCOM (Figure 3d), the maximum of horizontal advection and MLT tendency are both reduced by ~40%. Without horizontal advection by intraseasonal currents, the MLT maximum is reduced by 55% and occurs 2 days earlier. As in observations, the results from HYCOM suggest that intraseasonal ML currents associated with downwelling ER waves are critical to the amplification of warm SST anomalies. *Seiki et al.* [2013] observed during the CINDY/DYNAMO field campaign in the IO that horizontal advection by oceanic ER waves was important to the generation of intraseasonal SST variability responsible for modulating MJO initiation. The ML heat budget of *Seiki et al.* [2013] revealed that net surface fluxes and vertical entrainment could not fully account for the observed SST variability, similar to the results shown in Figure 3.

Figure 4 shows the 20–200 day band-pass filtered current anomalies and total SST/MLT from observations and HYCOM, respectively, at lag 0 days. The currents shown in Figure 4 are those that are suppressed in Figures 3c and 3d. In both composites, anomalous westward currents with maxima of 0.3 m s^{-1} are present across most of the equatorial western IO and predominantly located south of the equator. The intraseasonal currents associated with downwelling ER waves act on the temperature gradient to yield warm anomalies in the western IO, even in the presence of cooling by surface fluxes. The SST gradient is unique to the western IO and likely explains the preference for warm SST anomalies associated with ER waves to emerge there (see Figures 2c and 2d).

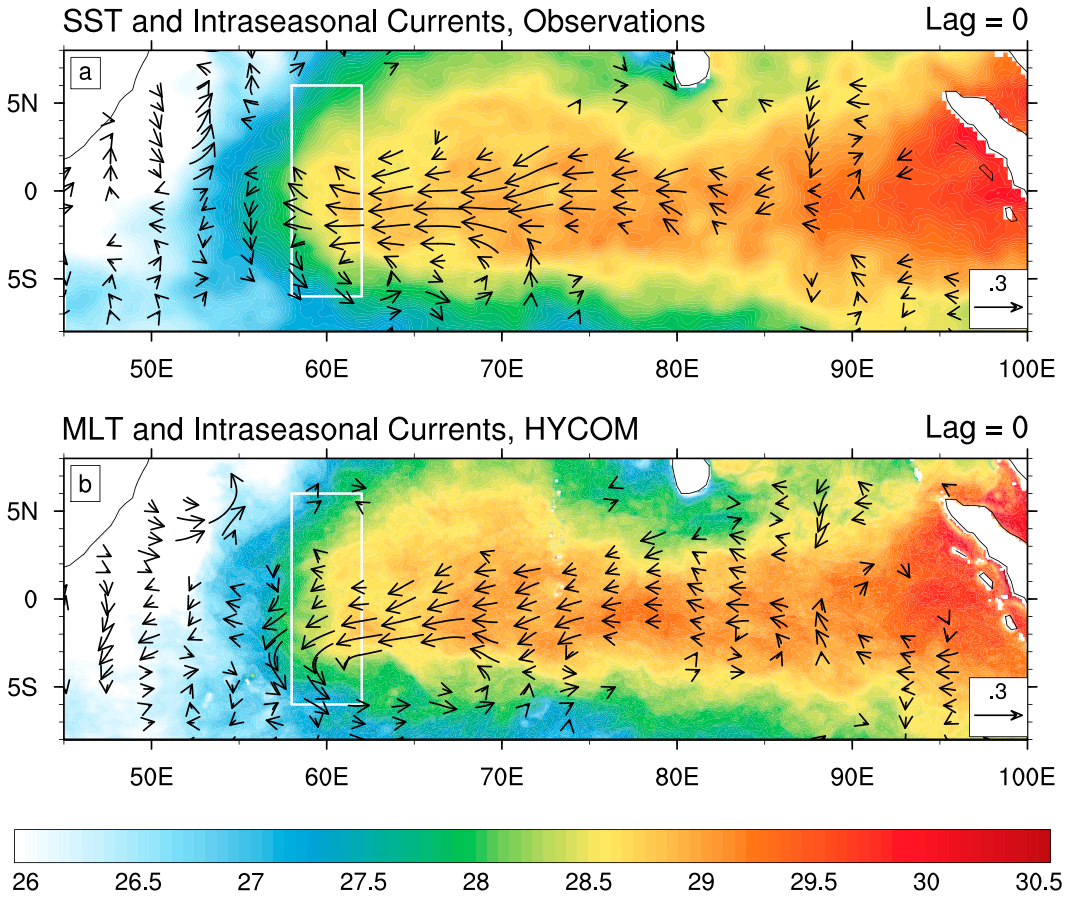

Figure 4. Composites of (a) 20–200 day band-pass filtered OSCAR current anomalies (vectors; m s^{-1}) and unfiltered NOAA SST (shading; °C) and (b) 20–200 day band-pass filtered HYCOM ML current anomalies (vectors; m s^{-1}) and unfiltered MLT (shading; °C) are shown for lag 0 days. Reference vectors are shown in the bottom right of each panel. The averaging box for the budget calculations is marked in white. Vectors less than 0.025 m s^{-1} are omitted.

5. Discussion

Processes regulating intraseasonal SST variability in the western IO are examined during periods of strong downwelling ER waves. SST warming associated with the arrival of downwelling ER waves in the western IO is hypothesized to be responsible for MJO convective onset by modulating SST gradients that, in turn, generate convergence in the atmospheric boundary layer and enhance surface heat fluxes [*Webber et al.*, 2010, 2012b; *Rydbeck and Jensen*, 2017]. Within this framework, identifying the processes responsible for SST warming enhances our understanding of MJO convective onset and may extend current MJO predictive capabilities.

Downwelling ER waves in the IO are linked to westward propagating, positive SSH anomalies located at 4°N/S and a westward jet along the equator. As the dowelling ER waves arrive in the western IO, warm SST anomalies of 0.12–0.15°C emerge near the leading edge of the westward jet. The phase relationship between convection and SST anomalies during MJO initiation in this study is unique. Warm SST anomalies are predominantly in phase with enhanced convection during convective onset in the western IO. Because the net surface flux is negative once convection begins, horizontal advection is largely responsible for the continued growth and maintenance of warm SST during this period.

The results of ML heat budgets for observations and reanalysis suggest that continued SST warming after convective onset is, to a large degree, accomplished by horizontal advection driven by currents associated with downwelling ER waves. These results support the remote forcing of warm SST anomalies in the western IO by downwelling ER waves and emphasize the need for properly resolving ER wave propagation and reemergence in coupled models. Horizontal advection derived from OSCAR currents should be interpreted

with caution as the meridional currents are in poorer agreement than zonal currents when compared to observations [i.e., *Johnson et al.*, 2007; *Sikhakolli et al.*, 2013]. This may partly account for discrepancies in the horizontal advection and residual terms of the respective budgets.

Robust downwelling ER waves in the western IO are linked to the generation of downwelling Kelvin waves in the western IO 75–90 days earlier [*Webber et al.*, 2010, 2012b; *Rydbeck and Jensen*, 2017]. The time required for ER waves to transit the IO suggests that MJO events initiated by downwelling ER waves are predictable at 10–13 week leads. Such lead times greatly exceed the current 3–6 week forecast capability of the MJO [e.g., *Neena et al.*, 2014; *Kim et al.*, 2014]. These results emphasize the need for fully coupled atmosphere-ocean modeling systems to gain predictive skill of MJO initiation. While not all MJO events that initiate in the western IO are associated with downwelling ER waves, we suppose that any process capable of growing and maintaining warm SST anomalies against cooling by the net surface flux might also stimulate MJO convection.

Acknowledgments
Thanks to Charlotte Demott and Jim Benedict for their helpful conversations that guided this work. This research is sponsored by the U.S. Office of Naval Research PISTON (73-4347-27-5) and NASCar (73-4347-34-5) projects. HYCOM + NCODA Reanalysis was funded by the U.S. Navy and the Modeling and Simulation Coordination Office (http://hycom.org). SSHs are produced by Ssalto/Duacs and distributed by AVISO, with support from CNES (http://www.aviso.altimetry.fr/duacs/). NOAA SST is provided by the NCEI (http://www.ncdc.noaa.gov/oisst). OSCAR currents are produced by ESR and hosted by JPL PODAAC (http://www.esr.org/oscar_index.html). TropFlux is collaboratively produced by LOCEAN from IPSL and NIO and supported by IRD (http://www.incois.gov.in/tropflux/). OLR is provided by NOAA/OAR/ESRL PSD (http://www.esrl.noaa.gov/psd/).

References

Bonjean, F., and G. S. E. Lagerloef (2002), Diagnostic model and analysis of the surface currents in the tropical Pacific Ocean, *J. Phys. Oceanogr.*, *32*, 2938–2954, doi:10.1175/1520-0485(2002)032<2938:DMAAOT>2.0.CO;2.

Cane, M. A., and E. S. Sarachik (1981), The response of a linear baroclinic equatorial ocean to periodic forcing, *J. Mar. Res.*, *39*, 651–693.

de Szoeke, S., J. Edson, J. Marion, C. Fairall, and L. Bariteau (2015), The MJO and air-sea interaction in TOGA COARE and DYNAMO, *J. Clim.*, *28*, 597–622, doi:10.1175/JCLI-D-14-00477.1.

Delcroix, T., J. Picaut, and G. Eldin (1991), Equatorial Kelvin and Rossby waves evidence in the Pacific Ocean through Geosat sea level and surface current anomalies, *J. Geophys. Res.*, *96*, 3249–3262, doi:10.1029/90JC01758.

Demott, C. A., J. J. Benedict, N. P. Klingaman, S. J. Woolnough, and D. A. Randall (2016), Diagnosing ocean feedbacks to the MJO: SST-modulated surface fluxes and the moist static energy budget, *J. Geophys. Res. Atmos.*, *121*, 8530–8373, doi:10.1002/2016JD025098.

Drushka, K., J. Sprintall, S. Gille, and S. Wijffels (2012), In situ observations of Madden-Julian Oscillation mixed layer dynamics in the Indian and western Pacific Oceans, *J. Clim.*, *25*, 2306–2328, doi:10.1175/JCLI-D-11-00203.1.

Earth Space Research (2009), OSCAR third degree resolution ocean surface currents. Ver. 1. PO.DAAC, CA, USA. Dataset accessed [2016-10-13] at doi:10.5067/OSCAR-03D01.

Gottschalck, J., P. Roundy, C. Schreck III, A. Vintzileos, and C. Zhang (2013), Large-scale atmospheric and oceanic conditions during the 2011–12 DYNAMO field campaign, *Mon. Weather Rev.*, *141*, 4173–4196, doi:10.1175/MWR-D-13-00022.1.

Gutzler, D. S., G. N. Kiladis, G. A. Meehl, K. M. Weickmann, and M. Wheeler (1994), The global climate of December 1992–February 1993. Part II: Large-scale variability across the tropical western Pacific during TOGA COARE, *J. Clim.*, *7*, 1606–1622, doi:10.1175/1520-0442(1994)007<1606:TGCODP>2.0.CO;2.

Halkides, D. J., D. E. Waliser, T. Lee, D. Menemenlis, and B. Guan (2015), Quantifying the processes controlling intraseasonal mixed-layer temperature variability in the tropical Indian Ocean, *J. Geophys. Res. Oceans*, *120*, 692–715, doi:10.1002/2014JC010139.

Han, W. Q., J. P. McCreary Jr., D. L. T. Anderson, and A. J. Mariano (1999), Dynamics of the eastern surface jets in the equatorial Indian Ocean, *J. Phys. Oceanogr.*, *29*(9), 2191–2209, doi:10.1175/1520-0485(1999)029<2191:DOTESJ>2.0.CO;2.

Jensen, T. G. (1993), Equatorial variability and resonance in a wind-driven Indian Ocean model, *J. Geophys. Res.*, *98*(C12), 22,533–22,552, doi:10.1029/93JC02565.

Jensen, T. G., T. Shinoda, S. Chen, and M. Flatau (2015), Ocean response to CINDY/DYNAMO MJOs in air-sea-coupled COAMPS, *J. Meteorol. Soc. Japan*, *93A*, 157–178.

Johnson, E., F. Bonjean, G. Lagerloef, J. Gunn, and G. Mitchum (2007), Validation and error analysis of OSCAR sea surface currents, *J. Atmos. Ocean. Technol.*, *24*, 688–701, doi:10.1175/JTECH1971.1.

Joseph, S., A. J. Wallcraft, T. G. Jensen, M. Ravichandran, S. S. C. Shenoi, and S. Nayak (2012), Weakening of spring Wyrtki jets in the Indian Ocean during 2006–2011, *J. Geophys. Res.*, *117*, C04012, doi:10.1029/2011JC007581.

Kim, H., P. Webster, V. Toma, and D. Kim (2014), Predictability and prediction skill of the MJO in two operational forecasting systems, *J. Clim.*, *27*, 5364–5378, doi:10.1175/JCLI-D-13-00480.1.

Knox, R. A. (1976), On a long series of measurements of Indian Ocean equatorial currents near Addu Atoll, *Deep Sea Res.*, *23*, 211–221.

Liebmann, B., and C. A. Smith (1996), Description of a complete (interpolated) outgoing longwave radiation dataset, *Bull. Am. Meteorol. Soc.*, *77*, 1275–1277.

Madden, R., and P. Julian (1972), Description of global-scale circulation cells in the tropics with a 40–50 day period, *J. Atmos. Sci.*, *29*, 1109–1123, doi:10.1175/1520-0469(1972)029<1109:DOGSCC>2.0.CO;2.

McPhaden, M. J. (1982), Variability in the central equatorial Indian Ocean. Part I: Ocean dynamics, *J. Mar. Res.*, *40*, 157–176.

Metzger, E. J., et al. (2014), US Navy operational global ocean and Arctic ice prediction systems, special issue on navy operational models, *Oceanography*, *27*(3), 32–43.

Moum, J., et al. (2014), Air-sea interactions from westerly wind bursts during the November 2011 MJO in the Indian Ocean, *Bull. Am. Meteorol. Soc.*, *95*, 1185–1199, doi:10.1175/BAMS-D-12-00225.1.

Neena, J., J. Lee, D. Waliser, B. Wang, and X. Jiang (2014), Predictability of the Madden-Julian Oscillation in the intraseasonal variability hindcast experiment (ISVHE), *J. Clim.*, *27*, 4531–4543, doi:10.1175/JCLI-D-13-00624.1.

Pacanowski, R. C., and S. M. Griffies, cited. (1998), MOM 3.0 manual. NOAA/GFDL. [Available online at http://www.gfdl.noaa.gov/smg/MOM/web/guide_parent/guide_ parent.html.]

Pascual, A., Y. Faugere, G. Larnicol, and P. Le Traon (2006), Improved description of the ocean mesoscale variability by combining four satellite altimeters, *Geophys. Res. Lett.*, *33*, L02611, doi:10.1029/2005GL024633.

Praveen Kumar, B., J. Vialard, M. Lengaigne, V. Murty, and M. McPhaden (2012), TropFlux: Air-sea fluxes for the global tropical oceans—Description and evaluation, *Clim. Dyn.*, *38*, 1521, doi:10.1007/s00382-011-1115-0.

Reynolds, R. W., T. M. Smith, C. Liu, D. B. Chelton, K. S. Casey, and M. G. Schlax (2007), Daily high-resolution-blended analyses for sea surface temperature, *J. Clim.*, *20*, 5473–5496, doi:10.1175/2007JCLI1824.1.

Ruppert, J., and R. Johnson (2014), Diurnally modulated cumulus moistening in the pre-onset stage of the Madden-Julian Oscillation during DYNAMO, *J. Atmos. Sci.*, *72*, 1622–1647, doi:10.1175/JAS-D-14-0218.1.

Rydbeck, A. V., and T. G. Jensen (2017), Oceanic impetus for convective onset of the Madden-Julian Oscillation in the western Indian Ocean, *J. Clim.*, doi:10.1175/JCLI-D-16-0595.1.

Saha, S., et al. (2010), The NCEP Climate Forecast System Reanalysis, *Bull. Am. Meteorol. Soc.*, *91*, 1015–1057, doi:10.1175/2010BAMS3001.1.

Seiki, A., M. Katsumata, T. Horii, T. Hasegawa, K. J. Richards, K. Yoneyama, and R. Shirooka (2013), Abrupt cooling associated with the oceanic Rossby wave and lateral advection during CINDY2011, *J. Geophys. Res. Oceans*, *118*, 5523–5535, doi:10.1002/jgrc.20381.

Sikhakolli, R., R. Sharma, S. Basu, et al. (2013), Evaluation of OSCAR ocean surface current product in the tropical Indian Ocean using in situ data, *J. Earth Syst. Sci.*, *122*, 187, doi:10.1007/s12040-012-0258-7.

Sperber, K. R., J. M. Slingo, P. M. Inness, and W. K.-M. Lau (1997), On the maintenance and initiation of the intraseasonal oscillation in the NCEP/NCAR reanalysis and in the GLA and UKMO AMIP simulations, *Clim. Dyn.*, *13*, 769–795, doi:10.1007/s003820050197.

Webber, B. G. M., A. J. Matthews, and K. J. Heywood (2010), A dynamical ocean feedback mechanism for the Madden-Julian Oscillation, *Q. J. R. Meteorol. Soc.*, *136*, 740–754, doi:10.1002/qj.604.

Webber, B., D. Stevens, A. Matthews, and K. Heywood (2012a), Dynamical ocean forcing of the Madden-Julian Oscillation at lead times of up to five months, *J. Clim.*, *25*, 2824–2842, doi:10.1175/JCLI-D-11-00268.1.

Webber, B., A. J. Matthews, K. J. Heywood, and D. P. Sterns (2012b), Ocean Rossby waves as a triggering mechanism for primary Madden-Julian events, *Q. J. R. Meteorol. Soc.*, *138*, 514–527, doi:10.1002/qj.936.

Wyrtki, K. (1973), An equatorial jet in the Indian Ocean, *Science*, *181*, 262–264, doi:10.1126/science.181.4096.262.

Yoshida, K. (1959), A theory of the Cromwell current and of the equatorial upwelling—An interpretation in a similarity to a coastal circulation, *J. Oceanogr. Soc. Jpn*, *15*, 159–170.